Mapping of Hydrothermally Altered Rocks using the Modified Spectral Angle Mapper (MSAM) Method and ASTER SWIR Data

Kodama, S.,[1] Takeda, I.,[2] and Yamaguchi, Y.,[3]
[1]Information Technology Research Institute, National Institute of Advanced Industrial Science and Technology, Central 2, Umezono 1-1-1, Tsukuba, Ibaraki 305-8568 Japan, E-mail: s.kodama@aist.go.jp
[2]Mitsubishi Materials Corporation, 3-2, Otemachi 1-chome, Chiyoda-ku, Tokyo 100-8117 Japan E-mail: itakeda@mmc.co.jp
[3]Department of Earth and Planetary Sciences, Nagoya University, Furo-cho, Chikusa-ku, Nagoya, 464-8601 Japan, E-mail: yasushi@nagoya-u.jp

Abstract
The shortwave infrared (SWIR) bands of the Advanced Spaceborne Thermal Emission and Reflection Radiometer (ASTER) target OH and CO_3^{2-} absorption features in the 2 μm region, in carbonate minerals and hydrothermal alteration minerals such as alunite, kaolinite, and calcite. We modified the Spectral Angle Mapper (SAM) method in order to use ASTER SWIR data to map hydrothermally altered rocks. The new method (Modified Spectral Angle Mapper: MSAM) provides a mineral index that is insensitive to the grain size of minerals and topography. The MSAM method can avoid misidentification due to mixture of the target mineral with different materials such as vegetation. The mineral index estimated from the simulated ASTER SWIR bands using the MSAM method shows greater variation among analyzed minerals than that obtained using the original SAM method. The mineral index images derived using the MSAM method exhibited a clear boundary between areas of contrasting mineralogy in the Cuprite region and Northern Grapevine Mountains region; this result is consistent with a previously published geologic map and hyperspectral data. Further investigation by the MSAM method identified several types of hydrothermal alteration zones associated with porphyry ore deposits near the Yerington District, Nevada. These results demonstrate the usefulness of ASTER SWIR data and the MSAM method in terms of lithologic mapping.

1. Introduction

The Advanced Spaceborne Thermal Emission and Reflection Radiometer (ASTER) is a multi-spectral imaging instrument with a high spatial resolution onboard NASA's Terra spacecraft that was launched in 1999 (Yamaguchi et al., 1998). The ASTER instrument has three spectral bands in the visible and near infrared (VNIR) regions, six in the shortwave infrared (SWIR) regions, and five in the thermal infrared (TIR) regions (Table 1). ASTER has a swath width of 60 km, which is larger than that of an airborne imager such as AVIRIS (Airborne Visible/Infrared Imaging Spectrometer; http://aviris.jpl.nasa.gov/). has already covered most of the land surface of the Earth with a spatial resolution of 15 m in VNIR bands, 30 m in SWIR bands, and 90 m in TIR bands. Such high spatial resolution multi-spectral images have a variety of applications such as in geology, agriculture, and in land use classification. The SWIR bands are especially useful in mapping hydrothermally altered rocks that contain clay and carbonate minerals, as these minerals have diagnostic spectral features in this spectral region (Figure 1). Various approaches that make use of multi-spectral images have been proposed to discriminate surface rock types, including spectral band ratios, spectral indices, and the spectral angle mapper (SAM) method. Band ratios are a simple approach and represent the most widely employed data-processing method; they have been used since the early stages of remote-sensing analysis (e.g. Rowan et al., 1976 and Abrams et al., 1977). Spectral indices are similar to principal component analysis (PCA) in the sense that both are orthogonal transformations of multi-spectral data, measuring the degree of similarity of spectral patterns by defining transform axes to represent specific spectral patterns of interest (Jackson, 1983). Yamaguchi and Naito (2003) proposed spectral indices for the discrimination and mapping of surface rock types by using the five SWIR bands of ASTER. This method was successfully applied to ASTER data from Cuprite in Nevada, USA (Yamaguchi and Takeda, 2003).

Table 1: Specifications of the ASTER instrument

	Band	Spectral range (μm)	Spatial resolution (m)	Quantization levels (bit)
VNIR	1	0.52-0.60	15	8
	2	0.63-0.69		
	3N	0.78-0.86		
	3B	0.78-0.86		
SWIR	4	1.600-1.700	30	8
	5	2.145-2.185		
	6	2.185-2.225		
	7	2.235-2.285		
	8	2.295-2.365		
	9	2.360-2.430		
TIR	10	8.125-8.475	90	12
	11	8.475-8.825		
	12	8.925-9.275		
	13	10.25-10.95		
	14	10.95-11.65		

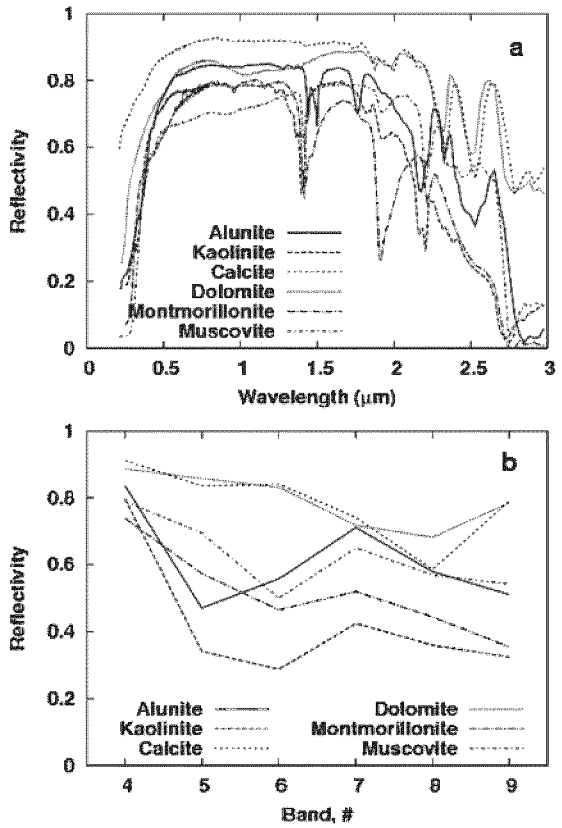

Figure 1: (a) Reflectance spectra of carbonate and clay minerals from Speclib Ver.5a, (b) Simulated ASTER SWIR spectra of the minerals listed in (a)

The SAM method measures the degree of similarity between image spectra and reference spectra by calculating the angle between spectra, treating them as vectors in n-space (Kruse et al., 1993a).

In this study, we modified the SAM algorithm and optimized it to the ASTER SWIR bands using simulated ASTER SWIR data derived from laboratory-determined spectra. We have proposed a Modified Spectral Angle Mapper (MSAM) method that removes topographic effects and suppresses the effect of the grain size of minerals. In addition, the vector space is expanded to the negative region (<0) in our algorithm; this enhances the differences in spectral angles between minerals, making it easier to discriminate different minerals using the MSAM method than when using the original SAM method. We applied the modified SAM method to ASTER SWIR data to map hydrothermally altered rocks in the Cuprite and Yerington regions, Nevada. The data used in this study is ASTER Level 2B05 data, which have been radiometrically and atmospherically corrected for surface reflectance (Yamaguchi et al., 1998 and Abrams, 2000). These data are available from the Japanese ASTER Ground Data System (Watanabe et al., 1995) and the Earth Observing System Data and Information System (http://spsosun.gsfc.nasa.gov/eosinfo/EOSDIS_Site/index.html).

2. Spectral Angle Mapper

The SAM method measures the degree of spectral similarity between the target material and a reference material (Kruse et al., 1993a). The reference spectrum is derived from field or laboratory measurements or from pixels in a spectral image. The SAM method measures the degree of similarity by calculating the angle between the two spectra, treating them as vectors in n-space. In the SAM algorithm, the spectral angle (θ) is defined as

the arc-cosine of the dot product of the vectors of the target mineral (***T***) and the reference mineral (***R***):

$$\theta = \cos^{-1}\left(\frac{\boldsymbol{T}\cdot\boldsymbol{R}}{|\boldsymbol{T}||\boldsymbol{R}|}\right)$$

Equation 1

The angle derived from the SAM method has a range of 0 to $\pi/2$, and is inversely proportional to the degree of similarity of the spectra. A smaller angle indicates greater similarity to the reference material. To ensure that the derived value is directly proportional to the degree of similarity, we have defined the mineral index (MI) as follows:

$$MI = 1 - \frac{\theta}{\pi/2}$$

Equation 2

Since the angle between two vectors is independent of the vector length, the SAM method is insensitive to the gain factor that arises due to the effects of topography and solar illumination.

3. Spectral Mapping using ASTER SWIR

Hydrothermal alteration minerals such as alunite or kaolinite and carbonate minerals such as calcite generally have a strong absorption in the 2.1–2.4 μm region due to the presence of OH^- and CO_3^{2-}. Figure 2 shows the spectral response of typical phyllosilicate and carbonate minerals to the ASTER SWIR bands (Bands 4 to 9). Carbonate minerals such as calcite and dolomite exhibit diagnostic absorption in Band 8, while other minerals have absorption peaks in Bands 5 or 6. In Band 9, calcite and dolomite show higher reflectance than other minerals. Reflectance is highest in Band 4 for all minerals. As stated above, the SAM method measures the degree of similarity between the spectral patterns of reference and target minerals. Therefore, it is desirable that the spectral pattern used in the SAM algorithm exhibits a large degree of variation among the analyzed minerals. In this study, we used Bands 5 to 9 for calculating the spectral angles. The reflectance spectra of rocks and minerals changes according to their grain size, even for rocks composed of a constant grain size. The spectral variation of rocks and minerals in response to grain size was evaluated by Hunt and Salisbury (1970, 1971) and Hunt et al., (1971). In these earlier studies, rocks and minerals were generally found to have higher reflectance and a shallower (flatter) depth of absorption with decreasing grain size. Figure 2 shows the spectral responses of calcite and dolomite to the ASTER SWIR bands for various grain sizes, as simulated from the spectra of Hunt and Salisbury (1971). The reflectance increases and shows a flatter spectral pattern as the particle size decreases, indicating that the vector to be used in SAM calculations changes in direction with variations in grain size; this result in a different spectral angle for different grain-sizes within the same mineral class, potentially leading to misclassification by the SAM method. Minerals can also be misidentified if they are mixed with vegetation; this misidentification arises due to their spectrally flat pattern in a short wavelength infrared region and the subsequent effect on the vector used in the SAM algorithm as outlined above. Figure 3 summarizes the mineral indices for carbonate and hydrothermal alteration minerals of various grain sizes. In several cases, the variation in index values among different grain sizes of a particular mineral is larger than that among different minerals (e.g. Figure 3a). As mentioned above, the spectral pattern of the ASTER SWIR bands becomes flatter with smaller particle size.

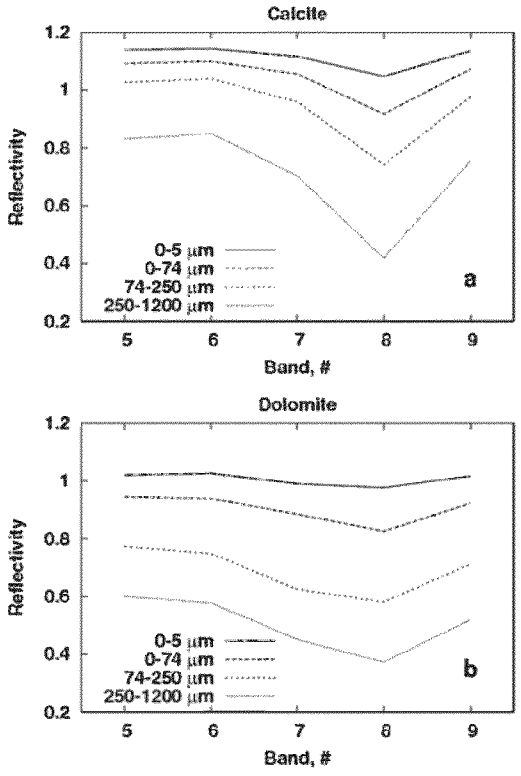

Figure 2: ASTER spectra for (a) calcite and (b) dolomite for various grain sizes. The absorption depths around Band 8 become shallower as the minerals become finer-grained. Data from Hunt and Salisbury (1971)

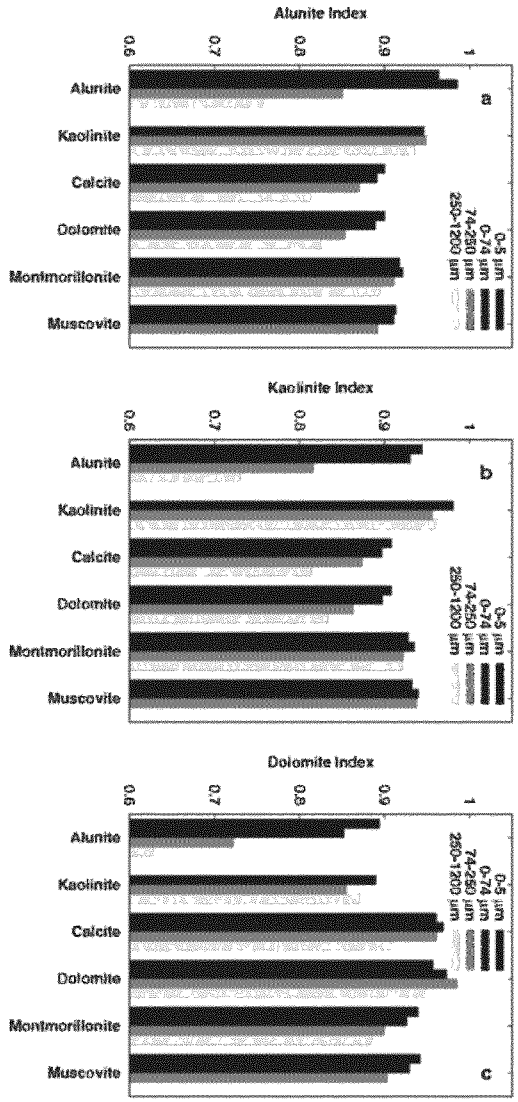

Figure 3: Mineral indices for carbonate and clay minerals of various grain sizes estimated using the SAM method. (a) Alunite index, (b) kaolinite index, and (c) dolomite index. Original data from Hunt and Salisbury (1970), Hunt and Salisbury (1971), and Hunt et al., (1971)

This trend leads to a greater degree of similarity between calcite and dolomite and other minerals (the spectral angles become close to an angle between the reference mineral and the optimized material with a flat spectrum), making it difficult to distinguish the target mineral from other minerals using the mineral index defined by the SAM method. To remove the effect of grain size and contamination of other materials such as silica (as found in sands) on the spectral angle, we introduce a new spectral parameter, $\boldsymbol{T'}$, which is derived from the spectral reflectance ($\boldsymbol{T}$) and the average reflectance of the spectrum (T_m):

$$\boldsymbol{T'}_{ij} = \boldsymbol{T}_{ij} - \boldsymbol{T}_{mj}, (\boldsymbol{T}_{mj} = \frac{\sum \boldsymbol{T}_{ij}}{N})$$

Equation 3

where i is a band number (i = 5–9), j is a pixel number in a spectral band image, and N is the total number of bands (N = 5 in this case). Figure 4 shows the modified spectral patterns ($\boldsymbol{T'}$) for the calcite spectra shown in Figure 3. The samples with different grain size exhibit a similar pattern, indicating that the grain size effect was successfully suppressed. In a vector space, $\boldsymbol{T'}$ deviates from a vector $\boldsymbol{T}_{fl}$, which has a flat spectral pattern of Tm, and is perpendicular to $\boldsymbol{T}_{fl}$ (Figure 5).

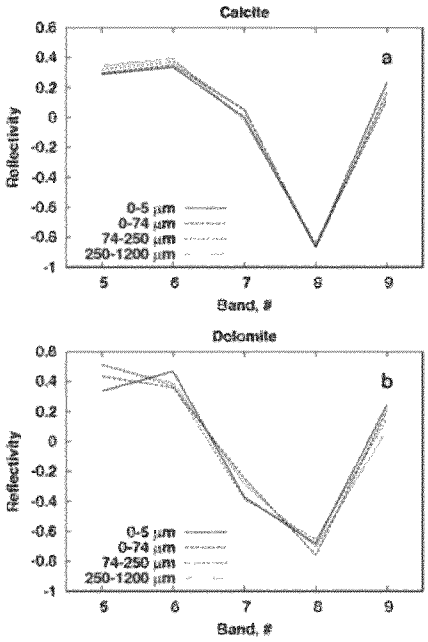

Figure 4: ASTER spectra of (a) calcite and (b) dolomite in Fig. 3 derived from Equation 3. The spectra are scaled relative to the average reflectance

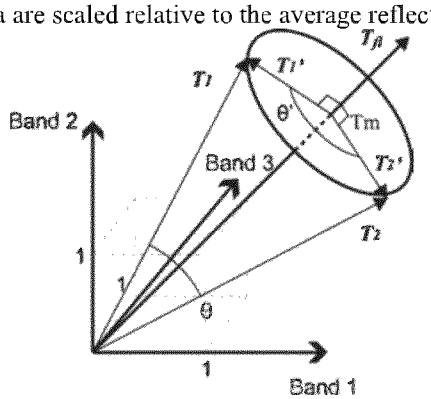

Figure 5: Schematic relationship of normal spectra (Tn) and residual spectra (Tn') in a vector space (consists of three bands). MSAM calculates the angle (θ') between T1' and T2', while SAM calculates the angle (θ) between T1 and T2

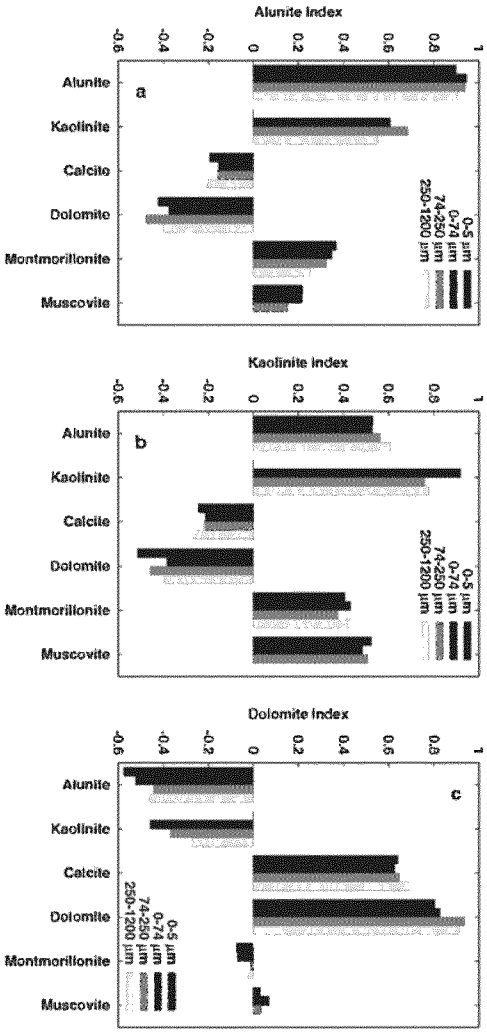

Figure 6: Mineral indices of carbonate and clay minerals of various grain sizes estimated using the MSAM method. (a) Alunite index,(b) kaolinite index, and (c) dolomite index. Original data from Hunt and Salisbury (1970), Hunt and Salisbury (1971), and Hunt et al., (1971)

The angle between $\boldsymbol{T}$ and $\boldsymbol{T}_{fl}$ decreases as the grain size decreases (approaches a flat spectral pattern); however, $\boldsymbol{T'}$ does not change its direction in response to variations in grain size, although its length is reduced. The same principle can be applied to minerals mixed with vegetation (or soils) as they have a spectrally flat pattern. By using $\boldsymbol{T'}$ instead of $\boldsymbol{T}$, we can estimate the angle between the target and reference minerals independently of grain size and free from contamination by vegetation. The MSAM method is also insensitive to the effects of solar illumination and topography as with SAM. In our algorithm, the vector space is expanded to the negative region, whereas in the original SAM method it is restricted to the positive region.

As a result, the spectral angle derived from the MSAM method has a range from 0 to π, corresponding to a range from –1 to 1 in the mineral index. Table 2 compares the mineral indices of the reference spectra (Figure 2) for the original SAM method and the MSAM method. The results derived from the MSAM method show a greater variation in each mineral index than those derived from the original SAM method, indicating that the MSAM method is more capable of discriminating between different minerals. Figure 6 shows the mineral indices for the samples used in Figure 4, as estimated using the MSAM method.

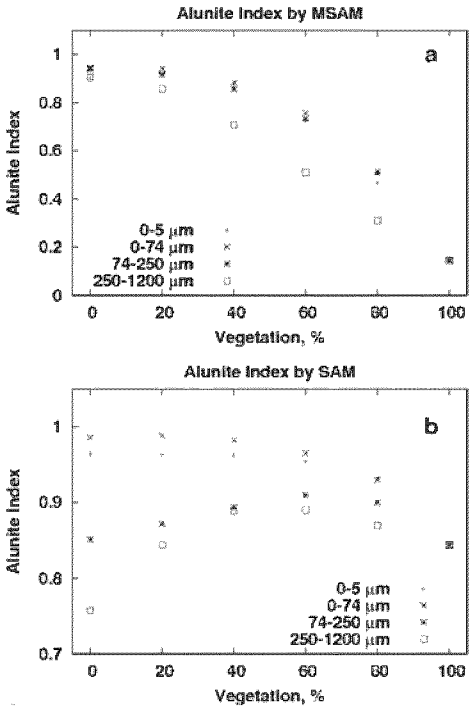

Figure 7: Comparison of alunite index between the indices from (a) MSAM and (b) SAM in response to the change in degree of vegetation mixture (0-100%) with the mineral

Compared to the indices estimated by the SAM method (Figure 4), the amount of variation in index values among the different minerals is larger for all indices. In addition, the amount of variation in index values among the different grain sizes of a particular mineral is smaller than that among different minerals, indicating that the MSAM method is able to successfully counter the effect of grain size. Figure 7 compares the result of (a) MSAM and (b) SAM when the minerals are mixed in with varying amounts of vegetation. The MSAM method exhibits a higher value for the target minerals than for vegetation, whereas the SAM method shows a lower value for the target minerals than for vegetation.

Table 2: Mineral indices estimated using MSAM and SAM

Reference Minerals	Mineral Indices by MSAM					
	Alunite	**Kaolinite**	**Calcite**	**Dolomite**	**Montmorillonite**	**Muscovite**
Alunite	1	0.531	-0.249	-0.477	0.071	0.039
Kaolinite	0.531	1	-0.300	-0.445	0.226	0.436
Calcite	-0.249	-0.300	1	0.732	0.143	0.034
Dolomite	-0.477	-0.445	0.732	1	0.179	0.046
Montmorillonite	0.071	0.226	0.143	0.179	1	0.563
Muscovite	0.039	0.436	0.034	0.046	0.563	1
Reference Minerals	**Mineral Indices by SAM**					
	Alunite	Kaolinite	Calcite	**Dolomite**	**Montmorillonite**	**Muscovite**
Alunite	1	0.937	0.859	0.865	0.873	0.885
Kaolinite	0.937	1	0.863	0.875	0.896	0.932
Calcite	0.859	0.863	1	0.964	0.889	0.894
Dolomite	0.865	0.875	0.964	1	0.902	0.910
Montmorillonite	0.873	0.896	0.889	0.902	1	0.938
Muscovite	0.885	0.932	0.894	0.910	0.938	1

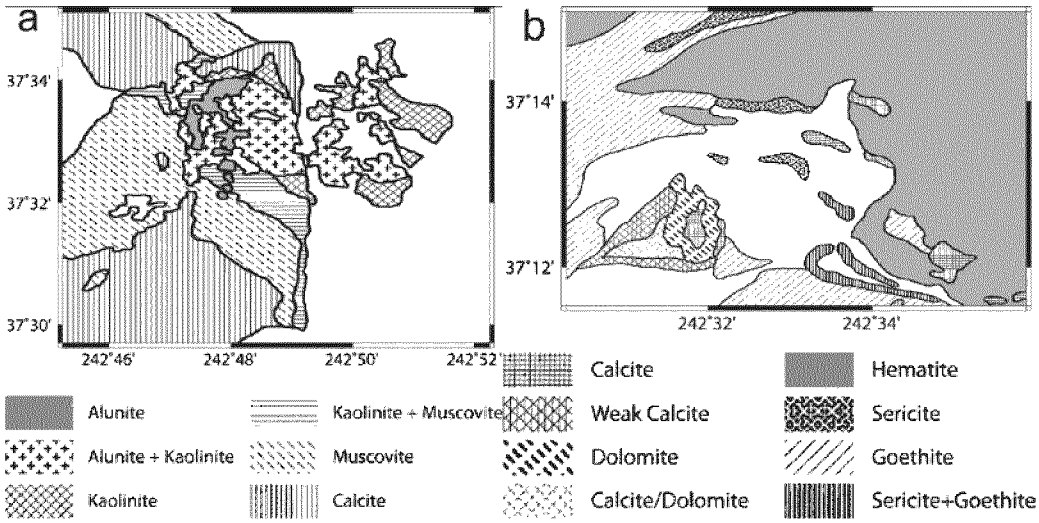

Figure 8: Mineralogical map of the (a) Cuprite region (from Clark and Swayze, 1996), and (b) NGM region derived from AVIRIS data (from Kruse et al., 1993)

4. Mapping at Cuprite and the Northern Grapevine Mountains using ASTER SWIR Data

To assess the applicability of the MSAM, method we have applied it to ASTER SWIR data acquired on June 29, 2004 for the Cuprite and Northern Grapevine Mountains (NGM) regions of Nevada, USA (Figure 8).

4.1 Geologic Setting

The Cuprite mining district is a major test site for evaluating the mineralogical mapping capability of airborne and spacecraft sensors; favored for its sparse vegetation coverage and variety of rock types, including volcanic rocks and sedimentary rocks such as limestone, sandstone, shale, and gypsum (e.g., Kruse et al., 1990 and Yamaguchi and Naito, 2003). Sections of Tertiary volcanic rock in this area were intensively altered during the Middle to Late Miocene. The altered rocks are termed (from most highly altered to least altered) silicified, opalized, and argillized. The dominant minerals are quartz in the silicified areas; opal, alunite, and kaolinite in the opalized areas; and kaolinite and montmorillonite in the argillized areas (Abrams et al., 1977 and Kruse et al., 1990). Clark and Swayze (1996) undertook detailed mineralogical mapping of this area using the AVIRIS instrument (Figure 8a). The NGM site is located approximately 50 km southwest of the Cuprite district, near the border of Nevada and California. Precambrian bedrock is exposed in this area (Moring, 1986). The Precambrian units include limestone, dolomite,

sandstone, and their contact metamorphic equivalents. Mesozoic plutonic rocks occur to the east of the Precambrian units, while Tertiary volcanic rocks are distributed to the north, west, and south. Kruse *et al.* (1993b) created a mineral map of this area using AVIRIS data. In their map, calcite and dolomite were detected within the Precambrian units, while sericite was identified in the Mesozoic plutonic units to the southeast (Figure 8b).

4.2 Results

Figure 9 shows mineral index images for alunite (a and d), kaolinite (b and e), and muscovite (c and f) in the Cuprite district, as derived from ASTER SWIR data. Figures 9a-c shows the results obtained by the MSAM method whereas Figures 9d-f shows those obtained by the original SAM method. In each image, the_maximum index value is stretched to white and 0 to black for MSAM, whereas the maximum index value is stretched to white and minimum to black for SAM. In the case of alunite indices, the indices derived by the MSAM method range from 0 to 0.922 whereas the indices derived by the SAM method range from 0.89 to 0.97. The alunite index from the SAM method is high not only in the alunite hills (0.94), but also in other alunite poor areas (mostly, >0.91). In contrast, the index from the MSAM method shows a low index value (<0.2) in the alunite poor area. For example, it is lower than 0.1 at the north of Cuprite (B in Figure 9a), and is less than 0 near the south border of the image (C in Figure 9a). Mean index values for these areas are summarized in Table 3. As a result of having large variation, an image derived by the MSAM method can exhibit a clear distribution of the target mineral. The kaolinite and muscovite images also have large variation (Table 3) and exhibit clear distributions (Figures 9b, c, e, and f). Figure 10 shows a color composite image consisting of the alunite, kaolinite, and muscovite indices. In the image, the alunite index is assigned to the color red, the kaolinite index to green, and the muscovite index to blue. We set a threshold value of 0.6 for alunite and 0.5 for kaolinite and muscovite. Only the pixels above threshold values are extracted and displayed on the image. Since the spectral pattern of alunite is similar to that of kaolinite, the kaolinite index yields relatively high values in alunite-rich areas, and vice versa (Figures 9a and b). The distribution of minerals is consistent with the mineral map in Figure 8, indicating that the threshold values worked well for extracting target minerals. Figure 11 compares the dolomite indices in the NGM region estimated by using the MSAM (Figure 11a) and SAM (Figure 11b) methods.

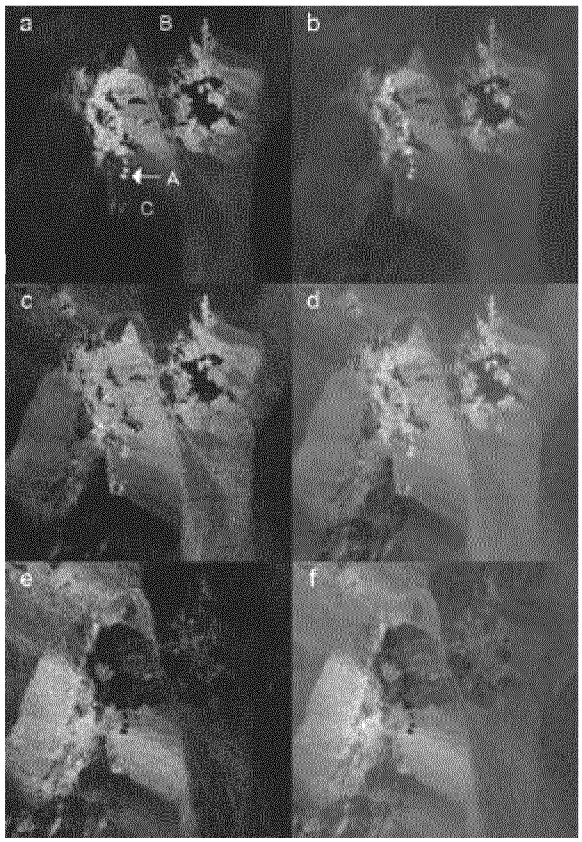

Figure 9: Mineral index maps of the Cuprite region obtained using (a–c) MSAM and (d–f) SAM; (a and d) alunite index, (b and e) kaolinite, and (c and f) muscovite. Each image was stretched using maximum and 0 for MSAM, and maximum and minimum for SAM

Table 3: Mineral indices determined for the Cuprite region

	A (5x5 pixels)		B (10x10 pixels)		C (10x10 pixels)	
	MSAM	**SAM**	**MSAM**	**SAM**	**MSAM**	**SAM**
Alunite Index	0.76	0.94	0.01	0.91	0	0.90
Kaolinite Index	0.58	0.95	0	0.92	0	0.92
Muscovite Index	0.03	0.89	0	0.89	0.09	0.89

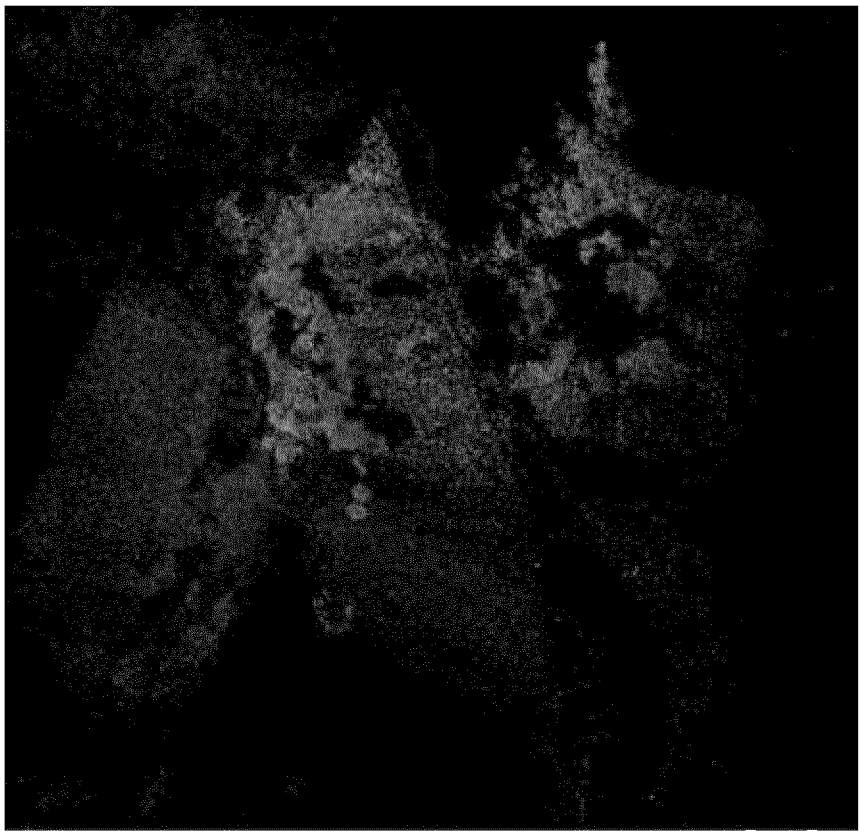

Figure 10: Color composites of mineral index maps of the Cuprite region obtained by using Modified SAM. The alunite index was assigned to the color red, kaolinite to green, and muscovite to blue. A threshold value of 0.6 was applied to the alunite index, and 0.5 to the kaolinite and muscovite indices

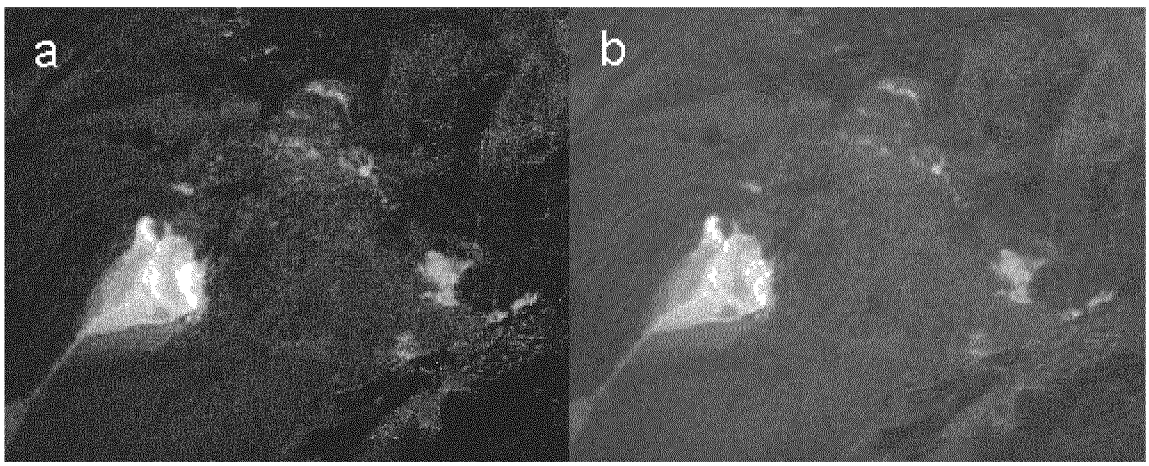

Figure 11: Dolomite index maps of the NGM region obtained by using (a) MSAM and (b) SAM. Each image was stretched using maximum and 0 for MSAM, and maximum and minimum for SAM

Images are stretched in the same manner as applied for Figure 9. The MSAM method shows a high index value (>0.7) in the dolomite area and a low index value (<0.2)for the non-dolomite area, while the SAM method shows an average value of 0.98 for the dolomite area and 0.95 for the non-dolomite area.

The MSAM method shows a large difference in the dolomite index between the dolomite area and the non-dolomite area. Figure 12 shows the distribution of calcite (colored red), dolomite (colored green), and sericite (colored blue) derived from the indices calculated by using the MSAM method.

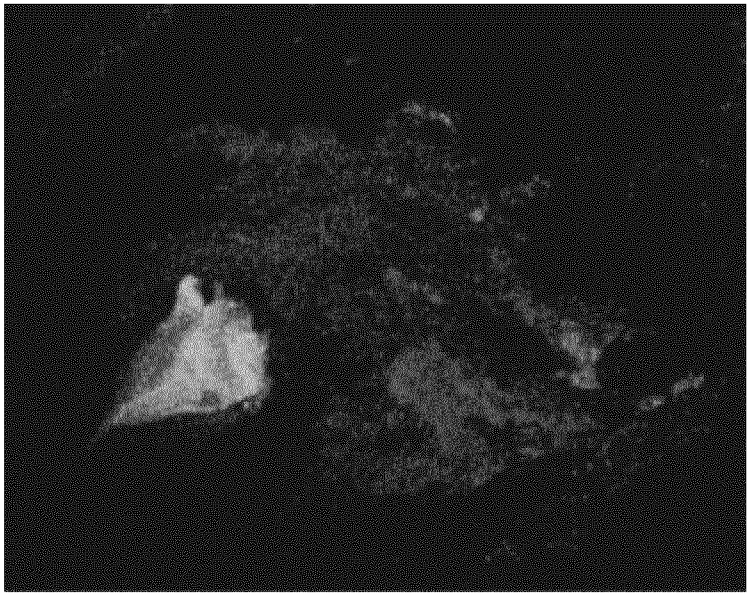

Figure 12: Color composites of mineral index maps of the NGM region obtained by using MSAM. A threshold value of 0.6 is used for calcite and dolomite, 0.4 for sericite

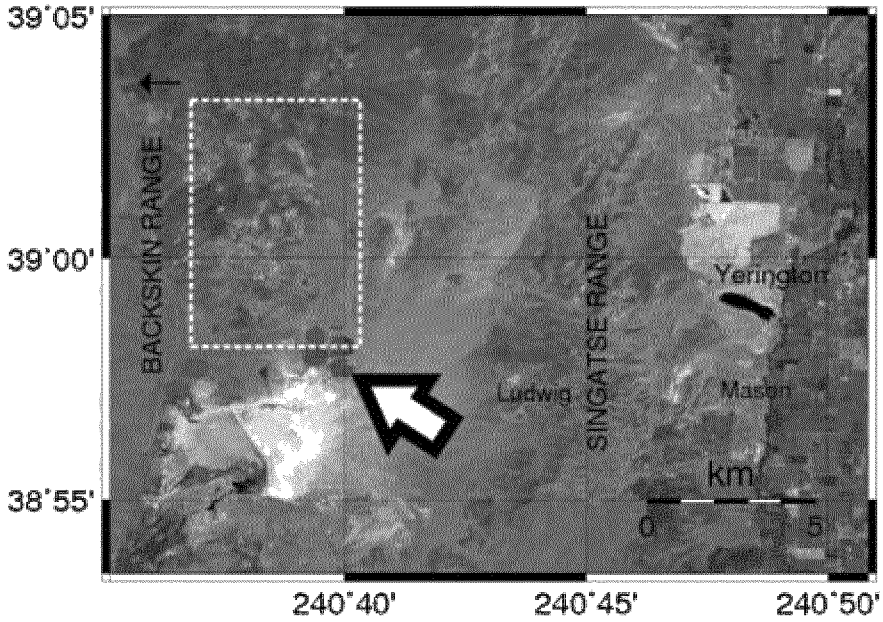

Figure 13: Color composite image of the Yerington District generated from ASTER VNIR data (Red: Band 3N, Green: Band 2, Blue: Band 1). The dashed square represents the area shown in Figure 17

In this image, calcite and dolomite were extracted using a threshold value of 0.6, while sericite was extracted using a threshold value of 0.4. Dolomite and calcite units including the 'calcite + dolomite' unit (colored dark red) and the 'weak calcite' unit (colored yellow to orange) in the southwestern part of the study area (Figure 11), are successfully identified by the MSAM method. Patches of calcite and sericite in the north- central and eastern part (Figure 11) are also clearly identified.

The results obtained for the Cuprite and NGM regions indicate that our new algorithm provides enhanced spectral angle maps that enable us to easily understand the distribution of minerals and identify areas that exhibit higher content of that mineral. We also conclude that ASTER data can be used to discriminate between hydrothermally altered and carbonate rocks, even though ASTER utilizes fewer bands than hyperspectral sensors such as AVIRIS.

5. Mapping of an Alteration Zone in the Yerington District, Nevada

5.1 Geologic Setting

The alteration zone in the Yerington District is located mainly between the Masson and Smith valleys, west of Yerington City (Figure 13). Early Mesozoic volcanic and sedimentary rocks are exposed in the southern Singatse Range from east of Ludwig to west of Mason (Figure 13). These rocks include Triassic andesite and rhyolite and Late Triassic to Early Jurassic pyroclastics and limestone. Two Middle Jurassic plutons, the Yerington batholith to the north and the Shamrock batholith to the south, intruded the Triassic to Early Jurassic volcanic and sedimentary rocks. The Yerington deposits were inclined and rotated to the west by about 90° as the result of Late Cenozoic normal faulting and a small additional component of pre-Oligocene deformation (Dilles, 1987). Tertiary volcanic rocks occur to the north of the Jurassic rocks, unconformable overlying the older geological units.

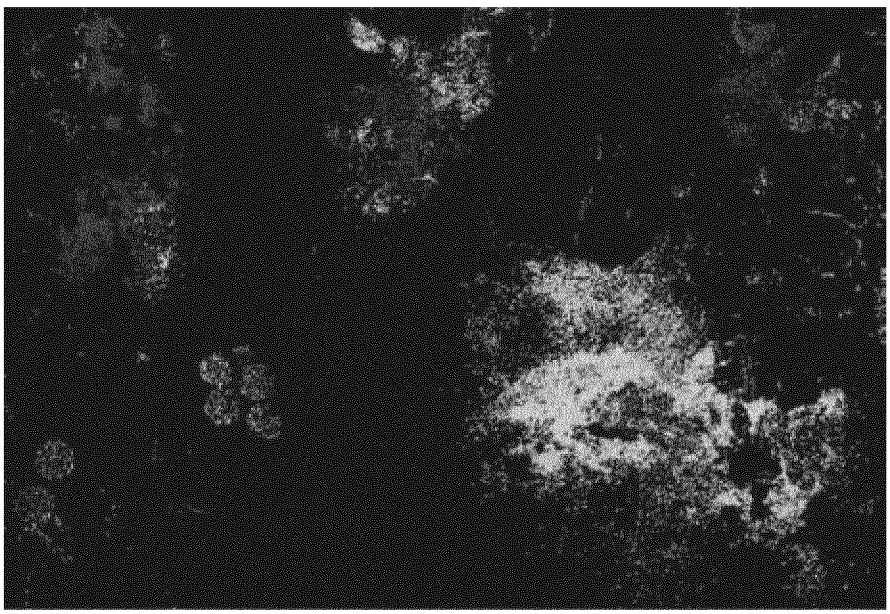

Figure 14: Color composite image of the calcite index (red), dolomite index (green), and montmorillonite index (blue) of the Yerington District. Threshold values of 0.8, 0.6, and 0.4 were applied respectively

Figure 15: Photograph of the silicified limestone area located on the east of Ludwig (Figure 13)

5.2 Results

Figure 14 shows a color composite image of the study area, in which the areas with a calcite index above the threshold value of 0.8 are colored red; a dolomite index above 0.6, green; and a montmorillonite index above 0.4, blue. Calcite and dolomite are identified (colored yellow-orange) in the south-central part of the image in the area located between the northern and southern Mesozoic batholiths near Ludwig (Figure 15). These minerals are also found in small patches to the northeast of the Triassic andesite and rhyolite units east of Ludwig, as well as around Quaternary basalt in the southeastern corner of the image. In the calcite index map derived by the SAM method, the vegetated area appears as high as the calcite-rich area near Ludwig (Figure 16). In contrast, the MSAM method exhibits a lower value in the vegetated area than that in the calcite-rich area, indicating that the MSAM method avoids mis-identification of minerals.

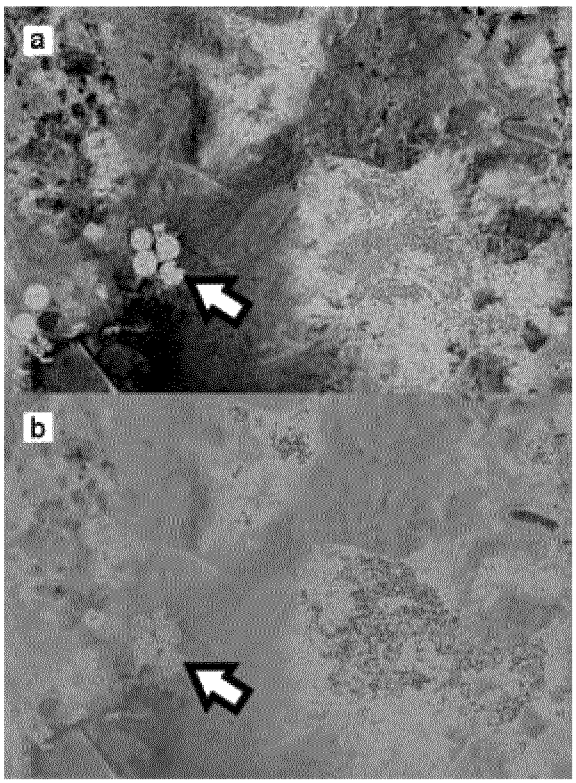

Figure 16: Calcite index map of the Yerington District obtained by using (a) MSAM and (b) SAM. Each image was stretched using maximum and 0 for MSAM, and maximum and minimum for SAM. Threshold value of 0.8 was applied to the index from MSAM, 0.95 to the index from SAM. Arrows indicate the location of vegetation rich area

The distribution of calcite interpreted from the mineral index map agrees well with the geologic map of Dilles (1987). Montmorillonite (colored blue) is identified in the upper left corner of Figure 14, where the Yerington batholith is indicated on the geologic map. Akiyama et al. (1989b) also reported montmorillonite in this area, based on spectral profiler mapping using GERIS data. We further investigated the Yerington deposits in the southern part of Buckskin Range, northwest of Smith Valley (Figure 13). This area comprises Mesozoic intrusive and sedimentary rock (Stewart and Carlson, 1977). We identified several different hydrothermal alteration minerals by applying the MSAM method to the ASTER SWIR data. Figure 17 shows a color index map of this region generated by assigning the alunite index to red, kaolinite index to green, and sericite to blue, with threshold values of 0.4, 0.5, and 0.6 respectively.

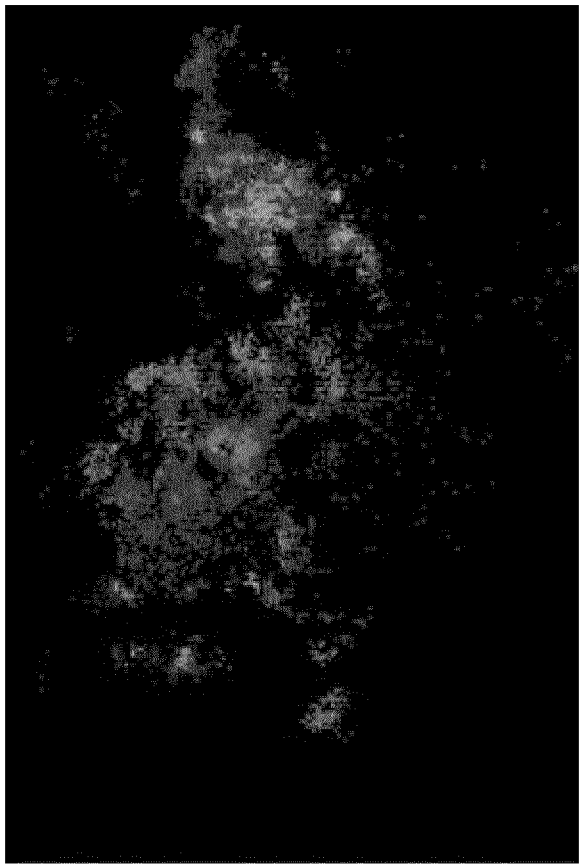

Figure 17: Color composite image of the alunite index (red), calcite index (green), and sericite index (blue) for an area near the Buckskin Range (dashed square in Fig. 13). Threshold values of 0.4, 0.5, and 0.6 were applied, respectively

Sericite is found in the lower central area of the image, while kaolinite and alunite occur around sericite-bearing rocks. According to Creasey (1959), hydrothermal alteration associated with porphyry copper deposits can be divided into four types: potassic alteration, phyllic alteration, argillic alteration, and propylitic alteration. Alunite and kaolinite are classified as representing argillic alteration, while sericite represents phyllic alteration. The distribution of argillic and phyllic minerals in Figure 16 indicates a zone of hydrothermal alteration associated with a porphyry ore deposit that resulted from the ascent of magmatic fluids from deeper levels (Lowell and Guilbert, 1970).

6. Summary

We modified the SAM algorithm and applied it to the ASTER SWIR bands. The new method (MSAM) estimates the angle between the vectors of two reflectance spectra, from which their mean reflectance values have been subtracted (see equation (3)). The mineral index derived by the MSAM method has a greater range (–1 to 1) than that derived by using the original SAM method (0 to 1), and it appears low enough for different materials including vegetation to discriminate from the target mineral using a threshold value. Vectors of the materials do not change their direction in response to variations in grain size, although their lengths vary; consequently, mineral indices derived from the MSAM method show a strong correlation with an abundance of these minerals and are insensitive to grain size and topography. In the Cuprite district and NGM region, the distribution of hydrothermal alteration minerals and carbonate minerals derived from ASTER SWIR data by using the MSAM method is consistent with the results of mapping using hyperspectral data. Carbonate minerals and montmorillonite were successfully mapped by the MSAM method in the Yerington District; the obtained results were consistent with the results of field mapping. We also identified several types of hydrothermal alteration associated with porphyry ore deposits within a Jurassic intrusive unit in the southern Buckskin Range, northwest of Smith Valley.

7. Conclusion

The strong agreement between our mineral mapping results in the Cuprite, NGM, and Yerington regions and those of previous studies undertaken using hyperspectral data demonstrates the usefulness of ASTER SWIR data in terms of geological mapping, and also demonstrate that our new method is applicable for the mapping of hydrothermally altered rocks. The application of the MSAM method can be extended to the visible-near infrared (VNIR) bands; this will enable more detailed surface mapping, including the mapping of iron oxides.

References

Abrams, M. J., Ashley, R. P., Rowan, L. C., Goetz, A. F. H., and Kahle, A. B., 1977, Mapping of Hydrothermal Alteration in the Cuprite Minig District, Nevada, Using Aircraft Scanner Images for the Spectral Region 0.46 to 2.36 μm, *Geology*, 5, 713-718.

Abrams, M., 2000, The Advanced Spaceborne Thermal Emission and Reflection Radiometer (ASTER): Data Products for the High Spatial Resolution Imager on NASA's EOS-AM1 Platform, *International Journal of Remote Sensing*, 21: 847-859.

Akiyama, Y., Komai, J., Yokoyama, T., and Okada, K., 1989, Digital Processing and Analysis Airborne Multispectral Data for Mapping Hydrothermal Alteration at Yerington, Nevada, *Proceedings of the 7th Thematic Conference on Remote Sensing for Exploration Geology*, Calgary, Alberta, Canada, 969-980.

Clark, R. N., and Swayze, G. A., 1996, Evolution in Imaging Spectroscopy Analysis and Sensor Signal-to-Noize: An Examination of How Far We Have Come, *The 6th Annual JPL Airborne Earth Science Workshop (http://speclab.cr.usgs.gov/PAPERS.imspec.evol/aviris.evolution.html)*

Clark, R. N., Swayze, G. A., Wise, R., Livo, K. E., Hoefen, T. M., Kokaly, R. F., and Sutley, S. J., 2003, *USGS Digital Spectral Library splib05a*, USGS Open File Report 03-395.

Dilles, J. H., 1987, Petrology of the Yerington Batholith, Nevada: Evidence for Evolution Porphyry Copper Ore Fluids, *Economic Geology*, 82, 1750-1789.

Hunt, G. R., and Salisbury, J. W., 1970, Visible and Near-Infrared Spectra of Minerals and Rocks: I Silicate Minerals, *Modern Geology*, 1, 283-300.

Hunt, G. R., and Salisbury, J. W., 1971, Visible and Near-Infrared Spectra of Minerals and Rocks: II. Carbonates, *Modern Geology*, 2, 23-30.

Hunt, G. R., Salisbury, J. W., and Lenhoff, C. J., 1971, Visible and Near-Infrared Spectra of Minerals and Rocks: IV Sulphides and Sulphates, *Modern Geology*, 3, 1-14.

Jackson, R. D., 1983, Spectral Indices in N-Space, *Remote Sensing of Environment*, 13, 409-421.

Kruse, F. A., Kierein-Young, K. S., and Boardman, J. W., 1990, Mineral Mapping at Cuprite, Nevada with a 63 Channel Imaging

Spectrometer, Photogramm. *Eng. Remote Sensing*, 56, 1, 83-92.

Kruse, F. A., Letkoff, A. B., Boardman, J. W., Heidebrecht, K. B., Shapiro, A. T., Barloon, P. J., and Goetz, A. F. H., 1993a, The Spectral Image Processing System (SIPS) – Interactive Visualization and Analysis of Imaging Spectrometer Data, *Remote Sensing of Environment*, 44, 145-163.

Kruse, F. A., Lefkoff, A. B., and Dietz, J. B., 1993b, Expert System-Based Mineral Mapping in Northern Death Valley, California/Nevada, using the Airborne Visible/Infrared Imaging Spectrometer (AVIRIS), *Remote Sensing of Environment*, 44, 309-336.

Lowell, J. G., and Guilbert, J. W., 1970, Lateral and Vertical Alteration-Mineralization Zoning in Porphyry Copper Deposits, *Economic Geology*, 7, 373-408.

Moring, B., 1986, Reconnaissance Surficial Geologic Map of Northern Death Valley, California and Nevada, U.S., *Geological Survey Miscellaneous Field Studies Map MF-1770*, U. S. Geological Survey, Washington, DC, 1:62,500.

Rowan, L. C., Wetlaufer, P. H., Goetz, A. F. H., Billingsley, F. C., and Stewart, J. H., 1974, Discrimination of Rock Types and Detection of Hydrothermally Altered Areas in South-Central Nevada by the use of Computer-Enhanced ERTS Images, *Professional Paper, 883*, U.S. Geological Survey, Reston, VA.

Yamaguchi, Y., Kahle, A. B., Tsu, H., Kawakami, T., and Pniel, M., 1998, Overview of Advanced Spaceborne Thermal Emission and Reflection Radiometer (ASTER), *IEEE Transactions on Geosicence and Remote Sensing*, 36, 4, 1062-1071.

Yamaguchi, Y., and Naito, C., 2003, Spectral Indices for Lithologic Discrimination and Mapping by using the ASTER SWIR Bands, *International Journal of Remote Sensing*, 24, 4311-4324.

Yamaguchi, Y., and Takeda, I., 2003, Mineral Mapping by ASTER in Cuprite, Nevada, USA, *Asian Journal of Geoinformatics*, 3, 3, 17-24.

Watanabe, H., Fujisada, H., and Sato, I., 1995, Preliminary Design Concept of ASTER Ground Data System, in *Proceedings of SPIE*, 2583, 26-40.